JOURNAL OF GEOPHYSICAL RESEARCH, VOL. 115, D07202, doi:10.1029/2009JD012520, 2010

Mineral dust observed with AERONET Sun photometer, Raman lidar, and in situ instruments during SAMUM 2006: Shape-independent particle properties

D. Müller,[1,2] B. Weinzierl,[3] A. Petzold,[3] K. Kandler,[4] A. Ansmann,[2] T. Müller,[2] M. Tesche,[2] V. Freudenthaler,[5] M. Esselborn,[3] B. Heese,[2] D. Althausen,[2] A. Schladitz,[2] S. Otto,[6] and P. Knippertz[7,8]

Received 20 May 2009; revised 8 September 2009; accepted 22 September 2009; published 10 April 2010.

[1] Aerosol Robotic Network (AERONET) Sun photometer observations were carried out at Ouarzazate, Morocco, during the Saharan Mineral Dust Experiment (SAMUM) 2006. Data from one measurement day, 19 May 2006, are used to derive particle optical and microphysical parameters with AERONET's latest version of light-scattering model for non-spherical particle geometry. In our analysis we also make use of a novel measurement channel at 1638 nm wavelength. We compare the results to data products obtained by airborne high-spectral-resolution lidar, several ground-based Raman lidar, and airborne and ground-based in situ measurement platforms. We chose that specific measurement day because the dust plume was vertically well mixed. Extinction coefficients from AERONET Sun photometer and lidar observations and in situ measurements agree well. Ångström exponents from Sun photometer and lidar are in close agreement, too. Airborne in situ measurements of dust particle size distributions show larger effective radii than inferred from the AERONET data. Complex refractive indices that are derived with the AERONET algorithm differ from the values obtained with different independent techniques employed in our study. The single-scattering albedo was derived from the airborne observations of particle size distributions and complex refractive indices. Single-scattering albedo differs to the value inferred from the AERONET data. The differences may be attributed to the different effective radii that we obtained from the various techniques. The differences between the data products from the various measurement platforms, however, cannot be generalized, as we could only test data for one measurement day. An analysis of additional measurements is under way.

Citation: Müller, D., et al. (2010), Mineral dust observed with AERONET Sun photometer, Raman lidar, and in situ instruments during SAMUM 2006: Shape-independent particle properties, *J. Geophys. Res.*, *115*, D07202, doi:10.1029/2009JD012520.

1. Introduction

[2] The Saharan Mineral Dust Experiment (SAMUM) aims at a better understanding of the radiative impact of mineral dust. In 2006 the first field mission was carried out in Morocco. Ouarzazate (30.93°N, 6.9°W, 1133 m above seal level (asl)) was the key site of the ground-based remote sensing instrumentation. Three Raman aerosol lidars and two Sun photometers were stationed at Ouarzazate airport [*Tesche et al.*, 2009; *Toledano et al.*, 2009]. The observations covered the time frame from 11 May until 10 June 2006. Airborne measurements with the Falcon aircraft were conducted between 18 May and 7 June 2006.

[3] One of the Sun photometers was an Aerosol Robotic Network (AERONET) system [*Holben et al.*, 1998]. Optical and microphysical properties of Saharan mineral dust were inferred from observations of direct and diffuse solar radiation and the use of AERONET's latest mineral dust model. That model has been specifically designed for the analysis of particles of non-spherical shape [*Dubovik et al.*, 2006]. We chose one measurement day as a case study for which we present some standard retrieval products of AERONET. Because of the complexity of the data set, we select only one measurement day for which we have a rather

[1]Presently at Atmospheric Remote Sensing Laboratory, Gwangju Institute of Science and Technology, Gwangju, South Korea.
[2]Leibniz Institute for Tropospheric Research, Leipzig, Germany.
[3]Institut für Physik der Atmosphäre, Deutsches Zentrum für Luft- und Raumfahrt, Wessling, Germany.
[4]Institut für Angewandte Geowissenschaften, Technische Universität Darmstadt, Darmstadt, Germany.
[5]Meteorological Institute, Ludwig Maximilian University, Munich, Germany.
[6]Institut für Methodik der Fernerkundung, Deutsches Zentrum für Luft- und Raumfahrt, Wessling, Germany.
[7]Institute for Atmospheric Physics, Johannes Gutenberg University of Mainz, Mainz, Germany.
[8]Now at School of Earth and Environment, University of Leeds, Leeds, UK.

0148-0227/10/2009JD012520

optimal data quality from all participating measurement platforms. On the basis of the lessons learned in this case study we will expand our studies to additional measurement days in a forthcoming publication. There we shall deal with the generalization of our findings in a more statistical manner.

[4] In this first contribution we present *shape-independent* dust particle properties. In the sense of our analysis techniques such *shape-independent* dust particle properties are properties that depend little on the specific choice of particle shape in the data retrieval algorithms. These parameters are light-extinction, light-scattering, and light-absorption coefficients. Furthermore, we infer particle size distribution, and thus particle effective radius, complex refractive index, and single-scattering albedo.

[5] In our second contribution [*Müller et al.*, 2010] we present parameters that depend in a strong way on particle shape, i.e., particle backscatter coefficients, particle lidar ratios, linear particle depolarization ratios, and axis ratios. In that regard this first paper can be considered as a comparably robust consistency check of dust parameters that are obtained with different measurement platforms and data analysis techniques, in which the specific choice of particle light-scattering model (sphere versus non-sphere) should be a minor source of uncertainty. In contrast our second part explicitly focuses on extracting inconsistencies of data products.

[6] The measurements with the AERONET instrument are particularly important. For the first time mineral dust was observed with an AERONET Sun photometer near a source region of Saharan dust while the same dust parameters were concurrently inferred from sophisticated remote sensing and ground-based and airborne in situ instrumentation operated at the location of the Sun photometer.

[7] In situ and laboratory measurements, and remote sensing results [*Heintzenberg*, 1978; *Nakajima et al.*, 1989; *West et al.*, 1997; *Volten et al.*, 2001; *Kaufman*, 1993; *Krotkov et al.*, 1999; *Liu et al.*, 1999; *Dubovik et al.*, 2002a; *Deuzé et al.*, 2000; *Sinyuk et al.*, 2003; *Müller et al.*, 2003; *Wand et al.*, 1999; *Herman et al.*, 2005; *Kalashnikova et al.*, 2005] reveal significant deviations in the light-scattering properties of natural desert dust particles compared to spherical-model particles [*Mishchenko et al.*, 2000]. As a result there have been numerous efforts to account for non-spherical particle shape in aerosol retrieval algorithms [*Kahn et al.*, 1997; *Dubovik et al.*, 2002b; *Mishchenko et al.*, 2003; *Herman et al.*, 2005; *Kalashnikova et al.*, 2005; *Liu et al.*, 1999]. *Kalashnikova and Sokolik* [2002, 2004] propose to model the optical properties by an ensemble of particles of non-spherical shape on the basis of geometrical particle parameters derived from in situ observations.

[8] *Dubovik et al.* [2002b] proposes the use of kernel look-up tables for simulating the single-particle optical properties of model spheroids. The mathematical basis in describing the light-scattering properties of spheroidal particles were adapted from *Mishchenko et al.* [1997]. Further modifications of the mineral dust model have recently been presented by *Dubovik et al.* [2006]. This updated model was validated with laboratory measurements of scattering matrices [*Volten et al.*, 2001]. The authors show that the optical properties determined from the scattering matrices are in good agreement with the same optical properties, if the spheroid model is applied to the measured particle size distributions [*Dubovik et al.*, 2006].

[9] Data from field studies are needed to corroborate the laboratory results. SAMUM offers us the unique opportunity to compare a multitude of data products derived by the AERONET inversion algorithm with the same quantities measured in situ and using lidar instruments near a source region of Saharan mineral dust. A series of papers can be found in the first special issue on SAMUM (*Tellus Series B*, *61*, 2009).

[10] *Toledano et al.* [2009] show a map indicating the locations of the two ground sites of the SAMUM instruments. Further information on the ground sites and the aircraft Falcon that was stationed in Casablanca is given by *Kandler et al.* [2009] and *Weinzierl et al.* [2009].

[11] Data were taken aboard the Falcon aircraft of the German Aerospace Center (DLR) during flights over the AERONET site [*Esselborn et al.*, 2009; *Petzold et al.*, 2009; *Weinzierl et al.*, 2009]. Dust was observed with several ground-based lidar systems at the AERONET site [*Freudenthaler et al.*, 2009; *Tesche et al.*, 2009]. In situ single-particle observations were carried out at ground near the village of Dunes du Tinfou [*Kandler et al.*, 2009; *Schladitz et al.*, 2009]. Tinfou, which is approximately 35 km southeast of the town of Zagora (30.23°N, 5.6°W), was the second field site during the SAMUM 2006 campaign.

[12] The location of Ouarzazate was well chosen for our study. The site is located near source regions where mineral dust is injected into the atmosphere. We observed nearly pure dust. As shown by *Kandler et al.* [2009] and *Weinzierl et al.* [2009] the concentration of anthropogenic pollution was negligible in the mineral dust plumes, because strong dust advection occurred in a sparsely populated environment. *Esselborn et al.* [2009] show on the basis of airborne lidar observations that the Atlas Mountain range which is located to the north and west of our field site, efficiently blocks the import of marine air from the North Atlantic Ocean as well as anthropogenic pollution from the densely populated areas of Casablanca and Marrakesh. For an example of such large-scale intrusion of marine air into the northwest of Morocco we refer to Figure 4 in the work of *Esselborn et al.* [2009].

[13] In section 2 we summarize the instruments and measurement methods used for the present study. In section 3 we present a brief overview of ensemble optical properties of dust plumes observed during the whole SAMUM period. In detail we present the results of a case study for the 19 May 2006 measurement. We compare the AERONET results to the findings from the other SAMUM platforms. We summarize our results in section 4 and close our contribution with an outlook in section 5.

2. Methodology

[14] A detailed description of instruments, data analysis, and error estimates is given in the papers of the first special issue on SAMUM (Tellus, Ser. B, 61, 2009). Here we only summarize those measurement techniques that are important

Table 1. Particle Parameters Compared in This Study[a]

	Platform							
	AERONET		Aircraft		Lidar		Ground	
Parameters	Direct	Indirect	Direct	Indirect	Direct	Indirect	Direct	Indirect
Extinction coefficient	x		x	x	x			x
Scattering coefficient		x		x				x
Absorption coefficient		x	x					x
Ångström exponents from extinction	x			x	x			
Ångström exponents from scattering		x		x				
Ångström exponents from absorption		x	x					
Extinction-to-backscatter (lidar) ratio		x	x	x	x			
Particle size distribution		x	x				x	
Complex refractive index		x		x				x
Single-scattering albedo		x		x				x

[a]Extinction coefficients and lidar ratio were determined aboard the Falcon directly with lidar and indirectly with in situ instrumentation. The results of the measurements at ground where made at the Tinfou site.

for this paper. Table 1 lists the parameters that are compared in our study.

2.1. AERONET Sun Photometer

[15] The AERONET Sun photometer was placed on the rooftop of one of the sea-containers that housed the lidar instrumentation at Ouarzazate airport. The automatic tracking Sun and sky radiometer is part of AERONET, which is a federated international network of Sun/sky radiometers [*Holben et al.*, 1998, 2001]. The instrument used in this study has been installed at the Leibniz Institute for Tropospheric Research (IfT) in 2001. The instrument was calibrated at NASA Goddard Space Flight Center (GSFC) in January 2005 before it was taken to Morocco. After the campaign the instrument was calibrated once more at GSFC in September 2006.

[16] Table 1 provides an overview on the data products that are derived with the AERONET Sun photometer and the inversion algorithm. The instrument measures the direct solar radiation at 339, 379, 441, 501, 675, 869, 940, 1021, and 1638 nm wavelength. From the signals optical depth is computed, except at 940 nm which is used to retrieve total precipitable water.

[17] The sky radiance (almucantar) measurements are done at 441, 675, 869, and 1021 nm. The data are used to retrieve aerosol phase function and particle size distribution [*Holben et al.*, 1998]. The inversion algorithm of *Dubovik and King* [2000] is used to retrieve the particle volume size distribution from 0.05 to 15 μm in radius, and the complex refractive index in the range from 1.33 to 1.6 (real part) and $0.0005i - 0.5i$ (imaginary part). A discussion on errors of the data products can be found in *Dubovik et al.* [2000].

[18] For the SAMUM campaign we additionally equipped the instrument with a novel measurement channel at 1638 nm. Adding data at this measurement wavelength is expected to increase the sensitivity of the AERONET algorithm with respect to the optical and microphysical properties of large aerosol particles. Another, and probably more important advantage of the novel channel is that it allows us to derive complex refractive index and single-scattering albedo at this infrared wavelength. However, at present, the accuracy of the calibration of this channel is generally worse than for the other channels in the visible spectrum, and AERONET quality assured retrievals are usually performed using only four standard channels (441, 675, 869, and 1021 nm). However, for this specific case study, the sky radiance measurements at 1638 nm were used. We emphasize that the use of this channel is not standard procedure. Because of the lower measurement accuracy of the 1638 nm channel, we present two sets of AERONET retrieval results: the standard AERONET product and the product that is derived using the new measurement channel. Thus we are able to demonstrate in how much the data products that are inferred with the use of the less-well calibrated channel differ from the data products that are inferred with the commonly applied measurement channels.

[19] The mineral dust model that is used for the analysis of our SAMUM data is described by *Dubovik et al.* [2006]. The model has been particularly designed for dealing with the optical properties of model particles of non-spherical shape. From the retrieved particle size distributions we compute effective radii, number, surface area, and volume concentrations. The complex refractive index, which is derived as a wavelength dependent quantity at 441, 675, 869, and 1021 nm, as well as the size distribution products are then used to calculate single-scattering albedo (scattering-to-extinction ratio).

[20] For all inversion calculations of the optical quantities we use the spheroid particle model and standard distributions of the aspect ratio as employed in the standard AERONET retrieval algorithm. The aspect ratio, the way it is used in this technique, is defined as the ratio of the longest axis of the assumed ellipsoids to their shortest axis and takes account of the orientation of the particles. In that way we obtain values <1 and >1, respectively. These standard distributions of the aspect ratio were obtained from inversion of data taken under laboratory conditions [*Dubovik et al.*, 2006].

2.2. Lidar Instruments

[21] Three Raman lidar instruments were operated at Ouarzazate airport, i.e., the Backscatter Extinction lidar-Ratio Temperature Humidity profiling Apparatus (BERTHA) of IfT [*Althausen et al.*, 2000; *Tesche et al.*, 2009], and the three-wavelength Multiwavelength Lidar System (MULIS) [*Freudenthaler et al.*, 2009] and the one-wavelength Portable Lidar Sytem (POLIS) [*Freudenthaler et al.*, 2009] of the University of Munich. Table 2 provides an overview on the data products that are measured with the instruments. For details of the data analysis procedure

Table 2. Particle Parameters Measured With the Four Lidar Systems[a]

	Backscatter Coefficient						Extinction Coefficient			Lidar Ratio			Linear Depolarization Ratio			
Instrument	355	400	532	710	800	1064	355	532	1064	355	532	1064	355	532	710	1064
BERTHA	x	x	x	x	x	x	x	x		x	x	°			x	
MULIS	x		x			x		x			x			x		
POLIS	x						x			x			x			
HSRL			x			x		x			x	°		x		x

[a]The lidar ratio at 1064 nm (circles) can only be estimated with the Klett method [*Ansmann and Müller*, 2005].

including a detailed error analysis we refer to *Tesche et al.* [2009] and *Freudenthaler et al.* [2009].

[22] Main reason for deploying three ground-based Raman lidar systems to Ouarzazate was the need to cover the atmospheric column as completely as possible. That allows us to compare the data from the Sun photometry to corresponding lidar quantities. For instance BERTHA does not provide trustworthy particle extinction profiles below a minimum height of 800–1000 m above ground. That effect is caused by the well known incomplete geometrical overlap between transmitted laser beam and field of view of the receiver telescope. The other two ground-based systems MULIS and POLIS provide extinction profiles as low as 800 m (532 nm; MULIS) and 250 m (355 nm; POLIS) above ground, respectively. Details on the minimum height of the different data products is given by *Tesche et al.* [2009].

[23] In the case of BERTHA, backscatter-coefficient profiles at 532 nm can be computed from signal ratios [*Tesche et al.*, 2009] also at daytime. The overlap effect widely cancels out, if signal ratios are taken, and the profile of the backscatter coefficient can be derived almost down to the ground.

[24] A fourth lidar system was operated aboard the Falcon aircraft of the DLR. This aircraft is a twin-engine jet aircraft that has a maximum flight altitude of 12.8 km asl. The aircraft was stationed at Casablanca international airport which is located approximately 280 km west of Ouarzazate.

[25] The airborne high-spectral-resolution lidar (HSRL) [*Grund and Eloranta*, 1990; *Eloranta*, 2005] is described by *Esselborn et al.* [2009]. The nadir-looking instrument measures profiles of particle backscatter, extinction and lidar ratio at 532 nm, as well as the linear particle depolarization ratio at 532 and 1064 nm. The data products of the HSRL are also presented in Table 2.

2.3. Airborne In Situ Observations

2.3.1. Instrumentation

[26] The SAMUM payload on board the Falcon combined the nadir-looking HSRL with instruments for in situ observations of aerosol particle microphysical and chemical properties. The instruments as well as calibration procedures are described in detail by *Weinzierl et al.* [2009].

[27] The aerosol absorption coefficient was measured with a 3-wavelength-Particle-Soot-Absorption-Photometer (PSAP) at the wavelengths of 467, 530, and 660 nm [*Virkkula et al.*, 2005]. The particle size distribution in the radius range from 0.002 to 50 μm was measured by a combination of several condensation particle counters operated at different cut-off radii; a differential mobility analyzer, a PCASP-100X, an FSSP-300 and an FSSP-100 instrument. Furthermore, the size distribution of nonvolatile aerosol compounds was recorded with three particle counters and a Grimm Model 1.109 optical particle counter combined with a thermal denuder.

[28] Apart from the wing-mounted PCASP-100X, FSSP-300, and FSSP-100, all instruments were operated inside the cabin of the Falcon. The inlet features determine the maximum particle radius measured inside the Falcon, which was approximately 1–1.5 μm.

2.3.2. Absorption Coefficient Retrieval

[29] The PSAP data and the simultaneously measured size distribution data were used to infer the complex refractive index from the spectral dependence of the measured absorption coefficient. The analysis of the PSAP data is subject of a paper by *Petzold et al.* [2009]. We only repeat the main step of retrieving the refractive index.

[30] Spectral aerosol optical properties can be calculated from size distribution measurements with the aid of an optical particle model. Here two Mie-scattering algorithms were applied, i.e., the algorithm by *Bohren and Huffman* [1983], which deals with spherical particles, and the algorithm by *Ackermann and Toon* [1981], which is used for describing the optical properties of coated spheres. Optical properties are simulated from 0.2 to 2 μm particle diameter and include the use of a look-up table of common spectral refractive indices. The numbers are taken from the literature. Spectral aerosol optical properties can be calculated for wavelengths from about 200 nm up to 20 μm. The calculations with the aerosol optical model require the assumption of a realistic chemical composition of the investigated particles. Details are given by *Petzold et al.* [2009].

[31] We calculate absorption coefficients which are compared with the PSAP measurements at the wavelengths 467, 530, and 660 nm. For this comparison, only the part of the particle size distribution that enters the PSAP ($r < 1.25$ μm) is considered in the aerosol optical model. The aerosol is assumed to consist of an exclusively light-scattering component, of one light-absorbing component with a weak spectral dependence of the absorption coefficient, and of one light-absorbing component with a strong spectral dependence of the absorption coefficient like hematite [*Petzold et al.*, 2009]. The refractive index of the mixed aerosol is determined by a volume mixing rule. If the inverted PSAP signal at 467, 530 and 660 nm agrees within 3% with the observed PSAP signal, we consider the match sufficient for the determination of refractive index, size distribution, and optical properties. Otherwise the iterative procedure is repeated by varying the relative contributions of the aerosol components.

[32] In the end we obtain effective refractive indices which then are used together with the complete size distributions (up to radii of 50 μm) to calculate the optical properties of the total aerosol size distribution. Variation

studies of the input parameters show that the imaginary part of the refractive index is determined with less than 25% uncertainty with the above described method [*Petzold et al.*, 2009]. The real part of the refractive index varies between 1.546 and 1.556.

2.3.3. Particle Shape Effects

[33] The fundamental error source in these calculations clearly is the assumption of spherical particle shape. However, we expect errors of only a few percent for data products that describe integral properties of the particles, i.e., particle extinction, scattering, and absorption coefficients, Ångström exponents calculated from these quantities, and single-scattering albedo [e.g., *Wiegner et al.*, 2009].

[34] The effect of particle non-sphericity on the particle sizing by light-scattering instruments was investigated in several studies. For dust-like particles, *Osborne et al.* [2008] show that in case of the PCASP which integrates light over a scattering angle range of 35°–120°, the effect on particle sizing is less than 10% to 20% with a tendency towards undersizing. In case of the FSSP 300 which integrates over a scattering angle range of 5°–12°, *Borrmann et al.* [2000] used T-matrix calculations of cirrus particles. The authors show that there is an oversizing for supermicrometer particles, if Mie-scattering theory is applied. *Lacis and Mishchenko* [1995] conclude from an analysis of particle scattering phase functions that extinction by non-spherical particles can be determined with acceptable accuracy by Mie theory.

[35] Summarizing, if we determine optical properties that are based on integrating particle phase function the errors can be kept low. Nevertheless the effect of particle asphericity on particle sizing has to be considered by careful quality assurance of the inverted particle size distributions.

2.3.4. Refractive Index Determination

[36] The refractive index was not only inferred from the PSAP measurements with aid of our optical particle model, but was independently derived from the chemical and mineralogical analysis of particles collected onboard the Falcon and a second aircraft, Partenavia [*Bierwirth et al.*, 2009], and at the Tinfou ground station. This analysis was performed on several thousands of individual particles by scanning electron microscopy. Details of the analysis technique are reported by *Kandler et al.* [2009]. On 19 May 2006, the refractive index could be determined for particle radii in the range from 0.05 to 1.25 μm (airborne) and from 0.05 to 12.5 μm (ground-based).

[37] For this particular day, approximately 12,900 individual particles were investigated. It turns out that the uncertainty in the real part of the complex refractive index is small, since the major components of mineral dust do not differ much in their real parts. The imaginary part has two significant sources of uncertainty, the presence of minute amounts of soot, and the uncertainty of the mineralogical phase composition of iron compounds and their distribution in the particle. The refractive index inversion of the PSAP data from the airborne samples [*Petzold et al.*, 2009] indicates the presence of an absorbing component with a spectrally flat wavelength dependence of the refractive index. This behavior corresponds either to soot or to kaolinite. However, the soot amounts required for the data inversion were <1% of total mass which is below the detection limit of the chemical analysis methods [*Kandler et al.*, 2009]. Therefore, soot is considered negligible for dust samples collected well above ground in the dust layers.

2.3.5. Extinction Coefficients

[38] We derive particle extinction, scattering, and absorption coefficients on the basis of the particle size distributions measured aboard the Falcon aircraft [*Weinzierl et al.*, 2009]. The uncertainty of the extinction coefficients is approximately 20%. This uncertainty is caused by the uncertainties of the refractive indices and the measured size distributions, and is confirmed by comparison with extinction coefficients measured with the HSRL at 532 nm [*Weinzierl et al.*, 2009]. According to the minor influence of particle non-sphericity on extinction coefficients [*Lacis and Mishchenko*, 1995] potential deviations of extinction coefficients at near-infrared wavelengths are most likely associated to uncertainties in the complex refractive index data that are taken from the literature and which are needed to calculate the optical parameters from size distributions.

2.4. Ground-Based Observations at Tinfou

[39] The most important data set that is used for our comparison study comes from the airborne measurements and the lidar instrumentation at Ouarzazate. We shall use, however, also results from observations at the Tinfou site, as they provide us with some important additional information on dust properties. The dust plume was vertically well mixed on 19 May 2006. Air transport on that day was from east to west. We assume that the dust conditions at Ouarzazate and Tinfou were similar.

[40] Particle number size distributions at Tinfou were determined with a combination of a Differential Mobility Particle Sizer (DMPS) and an Aerodynamic Particle Sizer (APS) inside a container laboratory. A detailed description of these instruments and the data evaluation is given by *Schladitz et al.* [2009]. The measurements cover the radius range from 10 nm to 5 μm (aerodynamic radius). Particles larger than 5 μm, respectively 3.8 μm of geometric radius were separated with a PM-10 inlet, which was mounted above the container roof. The complex refractive index is also derived from a chemical and mineralogical analysis of particles collected at the Tinfou ground station [*Kandler et al.*, 2009].

[41] The spectral particulate absorption coefficient and the imaginary part of the complex refractive index were also derived from measurements with a spectral optical absorption photometer (SOAP). Details of the method are discussed by *Müller et al.* [2009].

[42] SOAP provides the particle absorption coefficient on the basis of particles collected on a fiber filter and a radiative transfer model. The imaginary part of the complex refractive index then follows by using the absorption coefficient and the particle number size distributions measured downstream of the PM-10 inlet [*Schladitz et al.*, 2009], and applying an inversion code.

[43] A crucial constraint of this method is that the real part of the refractive index is set to 1.53 for all wavelengths. This assumption however seems justified. *Schladitz et al.* [2009] show that a real part of the refractive index of 1.53 gives the most reasonable results. We point out that lower real parts are derived with the AERONET algorithm.

[44] The error of the imaginary part is wavelength dependent and amounts on average to about 173% at 800 nm

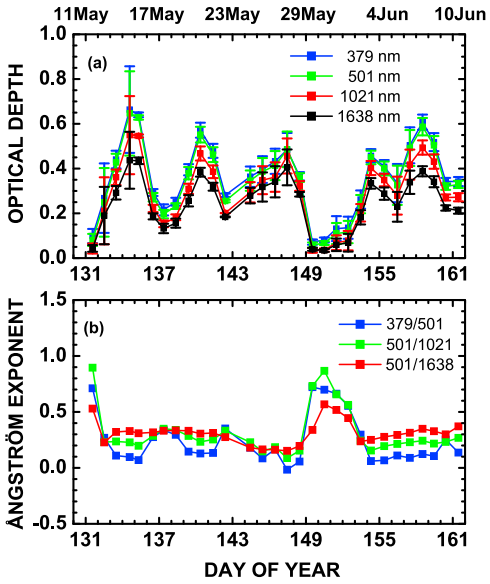

Figure 1. Time series of (a) dust optical depth measured at 379, 501, 1021, and 1638 nm from 11 May to 10 June 2006, and (b) Ångström exponents for the wavelength pairs 379/501 nm, 501/869 nm, and 501/1638 nm. Each symbol denotes the mean value of one measurement day. The error bars (one standard deviation) in Figure 1a denote the variation of the individual optical depth measurements on each day. We took between 3 and 43 individual measurements per day.

wavelength, 65% at 550 nm wavelength, and 53% at 400 nm wavelength. We varied the real part of the refractive index of 1.53 within ±5%. We consider that variation as a reasonable range of uncertainty in our analysis. A variation of ±5% generates an uncertainty of 3%–7% in the imaginary part, which is negligible in view of the other uncertainties.

3. Results

3.1. Time Series of Optical Depth and Ångström Exponents

[45] Figure 1 shows the time series of optical depth measured with the AERONET instrument during our 4-week field mission. A detailed discussion of optical depth is given by *Toledano et al.* [2009]. Daily mean optical depth at 501 nm varied from as low as 0.1 to maximum values of 0.65. Individual measurements show values as high as 0.8. That variation of optical depth occurred in pulse-like periods of approximately 6–7 days duration, during which optical depth increased to its maximum value and then decreased again.

[46] Figure 1 also shows the particle Ångström exponents calculated for three wavelength pairs. The numbers mostly vary between 0 and 0.4, which indicates relatively large particle radii. Only on a few days, characterized by low optical depths, the Ångström exponents are larger than 0.4, which indicates smaller particles. From the low optical depths on those days (around 0.1 at 501 nm) we estimate measurement uncertainties of the Ångström exponents [*Hamonou et al.*, 1999] of the order of 0.1 (absolute value) for the wavelength pair 380/501 nm. We suppose that there were nearly pure anthropogenic pollution conditions during those comparably short periods of low optical depth. Ouarzazate is located near the Draa Valley, which covers an area of approximately 23,000 km^2. The valley is a region of rather intense agricultural activity to the east of the Atlas mountain range. Traffic is considerably higher than in most other parts of southeastern Morocco. Yet small traces of dust are always present, and the presence of comparably few particles in the coarse mode fraction should lead to Ångström exponents smaller than 1. We did not carry out aircraft missions over Ouarzazate for further investigations of these clean aerosol situations.

3.2. Case Study, 19 May 2006: Profiles of Optical Properties

[47] We selected 19 May 2006 for our case study. On that day all measurement platforms acquired data. The Falcon aircraft carried out coordinated observations with our ground-based lidar systems.

[48] Sun photometer observations show that optical depth varied little during that day. Optical depth was 0.35 at 501 nm in the morning (0639 UTC) and peaked at 0.42 at noontime (1155 UTC). Those values are high enough for a trustworthy retrieval of particle microphysical properties with the AERONET inversion algorithm [*Dubovik et al.*, 2000].

[49] Time-height cross-sections of the dust plume were acquired with the HSRL between Casablanca and Ouarzazate. The dust was probed in situ during the ascent over Casablanca and the descent over Ouarzazate. Furthermore, the Falcon sampled dust in situ in the vicinity of Ouarzazate on constant-altitude sequences of about 10–15 min duration at altitudes of 3247 and 4853 m asl. These constant-altitude sequences were selected according to the vertical structure seen by the HSRL. The distance of closest approach between the Ouarzazate station and the Falcon transect was approximately 17 km during the overpass of the aircraft.

[50] Particularly the airborne observations with lidar allow us to check the horizontal and vertical homogeneity of the dust plume, in terms of optical particle properties, on a large spatial scale. We compare column-integrated properties derived from solar-pointing Sun photometry observations with (1) vertically resolved lidar observations, (2) line-like constant level airborne, and (3) point-like, ground-based in situ measurements.

[51] Figure 2 shows that the plume was rather well mixed along the flight path of the Falcon. We also show for illustration a time-height plot of the range-corrected backscatter signal (particles + molecules) taken with the IfT lidar at 1064 nm, and profiles of potential temperature and relative humidity acquired with radiosonde at the Ouarzazate field site. A detailed discussion of that measurement case and more examples are presented by *Tesche et al.* [2009].

[52] The time series shows that the plume did not change its vertical structure (expressed in terms of the range-corrected backscatter signal) at the field site during the period of interest. Traces of dust were detected to approximately 5 km asl in the morning hours. The top height of the dust layer increased to approximately 5.6 km asl in the evening. According to the profiles of potential temperature the dust plume was well-mixed. Relative humidity was low enough as to exclude any effects from particle growth.

[53] Clouds were not detected with the ground-based lidars during the time that we selected for our comparison

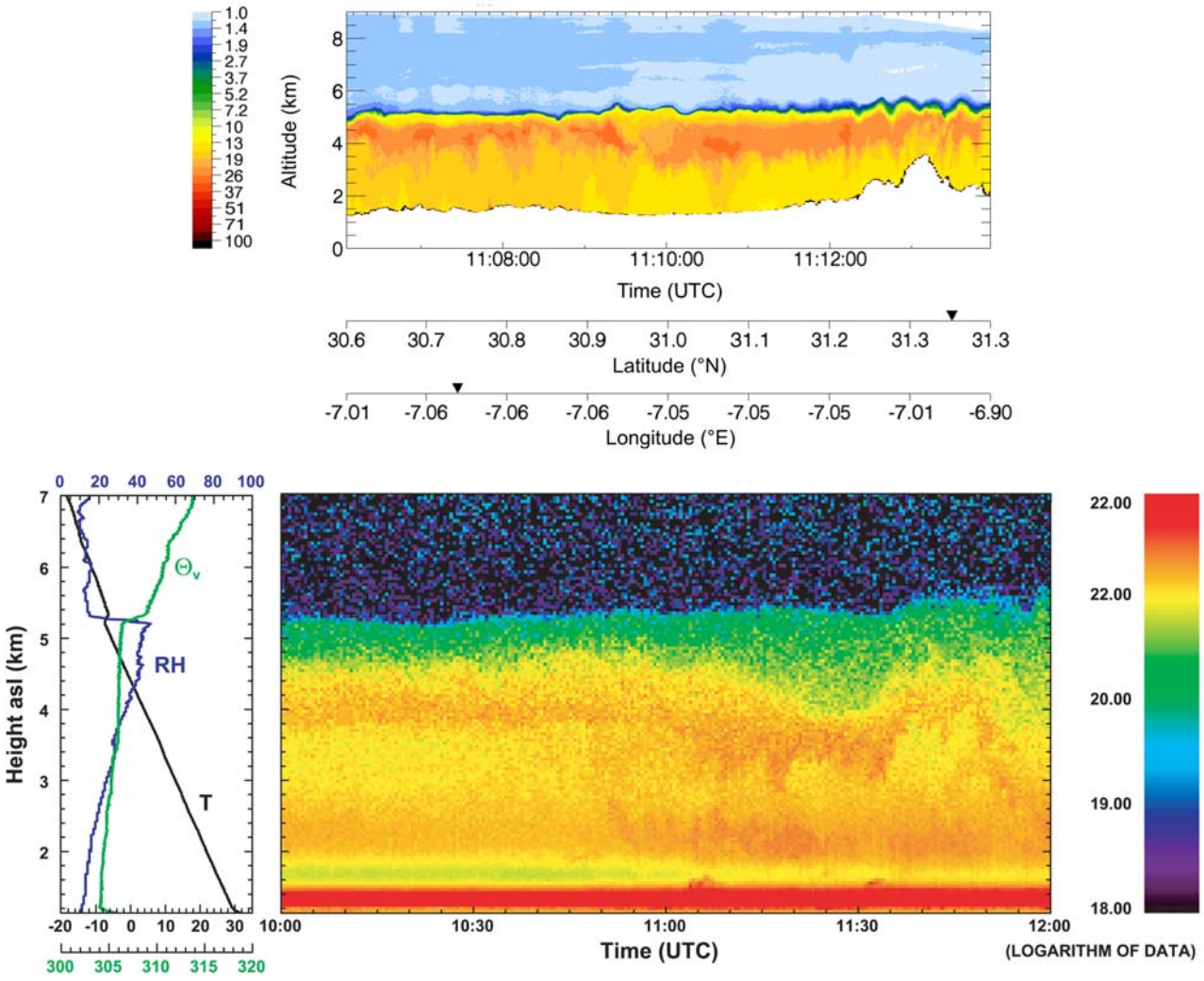

Figure 2. (top) Time-height variation of the range-corrected depolarization signal (particles plus molecules) at 1064 nm, measured along the flight leg indicated on the x axes. (bottom) Time-height variation of the range-corrected backscatter signal (particles plus molecules) at 1064 nm, measured with the six-wavelength lidar of IfT at Ouarzazate airport from 1000 to 1200 UTC on 19 May 2006. Single profiles were acquired with 30 s temporal resolution and 60 m vertical resolution. Also shown are profiles of relative humidity (RH), temperature (T) and virtual potential temperature (Θ_v). The data were taken with a radiosonde (Vaisala RS-92) launched at 1038 UTC at the Ouarzazate lidar station.

study (1000–1200 UTC). Visual inspection of the sky during the time of observations did not show clouds either. The cloud detection algorithm of the AERONET Sun photometer also did not indicate clouds. During the flight time 1106–1114 UTC the lidar signals of the airborne system did not indicate presence of clouds either.

[54] Figure 5 of *Tesche et al.* [2009] shows backward trajectory ensembles. Arrival heights of the airmasses are from the ground to 400 hPa at the Ouarzazate lidar station. The source region of the dust was located in Algeria and Libya. *Knippertz et al.* [2009] explain in detail possible mechanisms that may have led to the injection of dust. The authors identify cold surges from the Mediterranean Sea in association with eastward passing upper-level waves and lee cyclogeneses south of the Atlas Mountains as one main source of emission events. Other reasons are local emissions caused by a distinct cutoff low over northwestern Africa and gust fronts associated with dry thunderstorms over the Malian and Algerian Sahara.

[55] We can test the homogeneity of the dust plume along the vertical scale at the field site in much more detail on the basis of our four lidar systems. Figure 3 shows profiles of particle backscatter and extinction coefficients, Ångström exponents, lidar ratios and linear particle depolarization ratios at several wavelengths. Figure 3 gives us the strongest argument that a comparison of the various measurement platforms will not suffer from strong vertical and temporal changes of the dust plume properties.

[56] Particle backscatter profiles vary only little with height. We measured values around 1.5 Mm^{-1} sr^{-1} (1 Mm = 10^6 m = 10^3 km) below 3.5 km height asl, and slightly higher values up to 2.2 Mm^{-1} sr^{-1} around 4 km

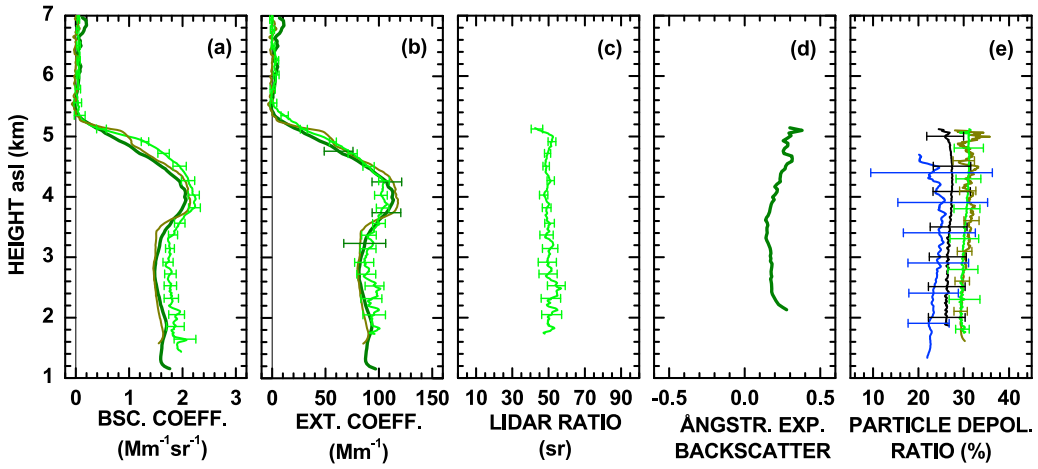

Figure 3. (a) Profiles of particle backscatter at 532 nm (BERTHA is dark green (thick line); HSRL is light green (thin line with error bars); MULIS is olive (thin line)) and (b) particle extinction coefficients at 532 nm measured with HSRL during the overpass over Ouarzazate and derived from BERTHA by multiplying the BERTHA-measured particle backscatter profile with 55 sr. (c) Profile of the particle lidar ratio at 532 nm. The profile was taken with HSRL. (d) Profile of the Ångström exponent calculated from the wavelength pair at 532/1064 nm of the particle backscatter coefficients (from BERTHA). (e) Profiles of the particle depolarization ratio at 355 nm (POLIS is blue), 532 nm (MULIS is olive; HSRL is light green), and 1064 nm (HSRL is black). Measurement times were from 1059 to 1119 UTC (POLIS), 1104 to 1114 UTC (MULIS), and 1109 to 1115 UTC (HSRL). During that measurement time the aircraft was in the area between 30.57°N and 31.2°N and between 7.0°W and 7.05°W. The mean flight altitude was 9.35 km asl. Uncertainty bars denote one standard deviation, except for the profiles of particle depolarization. A discussion on how the error bars for the latter case were derived is given by *Freudenthaler et al.* [2009]. The laser beams of MULIS and POLIS were tilted under 30°, and 2° off zenith, respectively. The laser beam of BERTHA was tilted under 45°.

height asl. The particle backscatter coefficient drops to negligible values around 5.2 km height asl. Extinction coefficients vary around 90 Mm^{-1} up to 3.5 km height asl. Above that height we find a layer with slightly higher extinction coefficients of up to 120 Mm^{-1}. We derive an optical depth of 0.35–0.37 at 532 nm wavelength from the different lidar instruments (BERTHA, HSRL, MULIS). The differences of the profiles in part can be attributed to different overlap correction functions that are applied to the various lidar instruments.

[57] Particle Ångström exponents are a function of particle size [*Ångström*, 1964]. Backscatter-related Ångström exponents for the wavelength pair at 532/1064 nm vary around 0.25 ± 0.1. This variation, keeping in mind measurement uncertainties of 20%–40%, corroborates the assumption of a comparably well-mixed dust plume.

[58] The lidar ratio depends on particle size, complex refractive index, and particle shape. The lidar ratio remains constant with height. We find mean values around 55 sr at 532 nm from the HSRL observations. Similar values are found from the ground-based lidar stations [see *Tesche et al.*, 2009]. A comparison of the measured lidar ratios to computations of the lidar ratio on the basis of AERONET retrieval products is presented in part two our paper [*Müller et al.*, 2010].

[59] The particle depolarization ratios are comparably constant throughout the investigated height range. A detailed overview on the linear depolarization ratio measurements is given by *Freudenthaler et al.* [2009].

[60] The height independence of the various profiles suggests that the particle complex refractive index did not vary significantly with height during the measurement time. This assumption is corroborated by the refractive index derived from the Falcon measurements [*Petzold et al.*, 2009] which show similar refractive indices (within 10%) at 3247 and 4853 m altitude asl.

[61] The finding that intensive dust optical parameters, i.e., particle Ångström exponents, lidar ratios, and depolarization ratios do not change with height is an important result. In that case we do not have to deal with averaging effects that may arise, if we want to compare column-mean values of intensive optical and microphysical particle properties from the Sun photometer inversion algorithm to respective quantities that we derive from our height-resolved lidar and in situ observations.

[62] Our second conclusion is that the height variation of the extensive optical parameters, i.e., particle backscatter and extinction coefficients must largely result from a height dependence of particle number concentration. Figure 3 shows that this variation is comparably low. The airborne measurements show that particle number concentration over Ouarzazate was slightly higher at 4 km height asl compared to the lower altitudes.

3.3. Microphysical Properties of Dust

[63] We obtain a highly complex picture of dust optical and microphysical properties. For that reason we apply a color-symbol-coded presentation to the results in all sections that follow. The colors and symbols are explained in

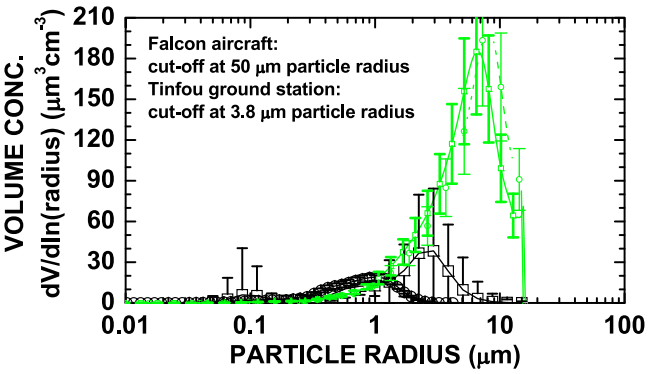

Figure 4. Particle volume size distributions (particle radius holds for volume-equivalent spherical particles) derived from AERONET Sun photometer measurements (squares) at four time steps (0649:19, 0711:50, 0801:35, and 0829:46 UTC) on 19 May 2006, measured aboard the Falcon aircraft during the overflight over the Sun photometer site at 3247 m asl (green circles) and 4853 m asl (green boxes) around 1107 UTC, and measured with in situ instruments at the Tinfou site from 0000 to 2400 UTC on 19 May 2006 (black circles).

the appendix. Briefly, different colors denote the different measurement platforms and/or techniques (Sun photometer, airborne lidar, ground-based lidar, airborne in situ, airborne single-particle analysis, ground-based single-particle analysis, SOAP at the ground). The symbols for each technique (same color) then denote different measurements times (Sun photometer measured several times on that day) or flight levels (aircraft) or size ranges (single-particle analysis with various cut-off radii).

3.3.1. Particle Size Distribution

[64] Mineral dust aerosol has a considerable fraction of coarse mode particles. The discussion of size distributions measured by different methods and on different platforms requires careful consideration of the cut-off properties of applied methods and inlet systems. The characteristic values of the respective inlet systems are briefly summarized before we present the results: The ground-based measurements of size distributions with a DMPS-APS combination used a PM-10 inlet, i.e., only particles with geometrical radii <3.8 μm were sampled. Ground-based measurements of size distributions from impactor samples cover a radius range of 2–250 μm. Airborne measurements of dust particles by means of optical particle counters are limited to maximum radii of 50 μm. Most important, the comparison of ground-based DMPS-APS data with data from impactor analyses and from airborne measurements has to consider the fact that the DMPS-APS size distributions miss the major part of the coarse mode fraction of the dust size distributions. In contrast, the AERONET algorithm retrieves particles with radii as large as 15 μm. The minimum particle radius considered in the retrieval is 0.05 μm.

[65] Figure 4 shows particle volume size distributions derived with Sun photometer, measured aboard the Falcon aircraft, and measured at the Tinfou site. It must be stated very clearly that we only present the Tinfou results because these data show us the fine mode fraction (anthropogenic pollution), but not the coarse mode fraction of the size distribution. These measurements serve as a comparison to the fine mode fraction retrieved with the Sun photometer.

[66] The AERONET observations did not show a significant change of optical depth between 0649 UTC (start of Sun photometer measurements) and 1107 UTC (overflight of the Falcon aircraft). The uncertainty bars of the AERONET results denote the variation (in terms of one-standard deviation) of the mean values retrieved for the four time steps.

[67] The size distributions from Falcon represent the average of a 5 min measurement time, which is equivalent to a horizontal distance of approximately 60 km. We point out that the size distributions shown here slightly differ from the parameterized particle size distributions shown in Table 4 of *Weinzierl et al.* [2009]. The data presented here were screened once more in a quality test.

[68] The size distribution at the Tinfou site represents the mean of 48 individual measurements on 19 May 2006. The uncertainty bars describe the variation of the individual size distributions (mean value) in terms of one-standard deviation.

[69] As stated before we detected particles up to 50 μm geometrical radius with the airborne instruments. The difference in the upper cutoff sizes, compared to the ground-based measurements, is the main cause of the differences in the volume size distributions observed at Tinfou and aboard the Falcon aircraft. Comparisons with ground-based measurements on the basis of single-particle analysis of the entire size range show close agreement between data from Tinfou and from the Falcon platform [*Weinzierl et al.*, 2009].

[70] AERONET and Falcon resolve well the coarse mode fraction of the volume size distribution above approximately 0.5 μm particle radius. But with regard to the large particles there is a gross difference between the AERONET and the Falcon data. The distributions provided by the Falcon aircraft are shifted to larger particle radii compared to what we obtain from the AERONET measurements. Furthermore the peak value of the volume size distribution is considerably higher compared to the peak that is obtained from the AERONET retrieval.

[71] The reason for this inconsistency is not clear. On the one hand, *Dubovik et al.* [2006] present results of dust particle size distributions that agree well to data from laboratory measurements. Results on dust size distributions are also presented by *Dubovik et al.* [2002a].

[72] On the other hand similar differences regarding mineral dust size distributions are reported by *McConnell et al.* [2008] for the Dust Outflow and Deposition to the Ocean (DODO) experiment. The authors compare size distributions measured in situ with optical spectrometers and size distributions retrieved from AERONET measurements. Both methods show reasonable agreement for particles in the accumulation mode at radii greater than 0.2 μm. However, a lower number of particles in the coarse mode fraction was derived with the AERONET algorithm compared to what was obtained from observations with the optical spectrometers, see Figure 7 in *McConnell et al.* [2008].

[73] The measurements aboard the Falcon aircraft did not indicate any significant contribution of particles with radius >15 μm on that day. The term significant means that the measurement signals were below the detection limit of 10^{-2} of the optical particle counters. Significant number concentrations of particles with radius >15 μm were detected

Table 3. Parameters of Particle Size Distributions Measured Aboard the Falcon Aircraft, and Derived With the Retrieval Algorithm of AERONET[a]

	Total Size Distribution			Coarse Mode (Radius > 0.5 μm)			Fine Mode (Radius < 0.5 μm)			
		Falcon			Falcon			Falcon		
	AERONET Column	3247 m	4853 m	AERONET Column	3247 m	4853 m	AERONET Column	3247 m	4853 m	Tinfou Ground
r_{eff} (μm)	0.65	3.4	3.2	1.62	4.3	3.8	0.12	0.21	0.23	0.23
n_{tot} (1/cm^3)	1754	680	439	7.5	6	7	1746	675	432	516
a_{tot} (μm^2/cm^3)	268	232	241	94	181	199	175	52	44	49
v_{tot} (μm^3/cm^3)	58	265	256	51	261	253	7	3.5	3.3	3.7

[a]We show the results for the total particle size distribution, for the particles in the coarse mode fraction, and for the fine mode fraction. The parameters from AERONET represent the mean of the results acquired from observations at 0649:19, 0711:50, 0801:35, and 0829:46 UTC on 19 May 2006. The dust layer extended from station elevation (1150 m) to 4750 m, which is equivalent to a geometrical depth of 3600 m of the dust layer, see Figure 3. The parameter r_{eff} denotes effective radius. The term v_{tot} denotes volume concentration of the particle size distribution. The expression a_{tot} denotes the surface-area concentration, and n_{tot} is the number concentration of the particle size distribution. The flight altitude of the aircraft was 3247 and 4853 m asl. With regard to the Falcon data and the data taken at Tinfou we use 0.5 μm particle radius as separator for the fine mode and the coarse mode fraction. Minimum particle radius is 10 nm for the measurements at Tinfou. The coarse mode fraction of the aircraft data consists of particles in the radius range from 0.5 to 14.9 μm (3247 m asl) and from 0.5 to 15.5 μm (4853 m asl). Minimum particle radius is 7.5 nm for the measurements aboard the Falcon.

during measurement flights on other days [*Weinzierl et al.*, 2009]. For this reason we think we can exclude the possibility that the cut-off of 15 μm particle radius which is used in the AERONET inversion algorithm may be a reason for the observed differences.

[74] At first look the results for the fine mode fraction observed with AERONET and the in situ platforms (Falcon, Tinfou) agree acceptably well. We find a low concentration of particles in the fine mode fraction of the size distribution. Table 3 summarizes the results for the measured particle size distributions in more detail. Shown are the results for particle effective radius, and number and surface-area and volume concentration. We must consider that the different measurement platforms possess variable sensitivity to the different particle sizes. For that reason the numbers in Table 3 are given for different parts of the particle size distribution. The AERONET and Falcon observations deliver very different values for the four parameters, depending on the size range that is used in the calculation of the parameters.

[75] Particle effective radius derived from the AERONET observations for the total particle size distribution (15 μm maximum particle radius) is about a factor 5 lower than the value that we obtain from the Falcon measurements (also 15 μm maximum particle radius). Number concentration from AERONET is about a factor 3 higher than number concentration from the Falcon measurements. Surface-area concentration differs by about 15%. Volume concentration from AERONET is a factor four lower than volume concentration measured aboard the Falcon aircraft.

[76] With regard to the effective radius of the coarse mode fraction of the particle size distribution, which we define in this study for particles with radii above 0.5 μm, we find a factor 2.5 difference from AERONET and Falcon measurements. Number concentration in that case is similar, but again volume concentration differs.

[77] If we only look at the fine mode fraction (particles with radii <0.5 μm) we find a factor 2 difference for effective radius. The AERONET retrieval delivers nearly a factor 3 higher number concentration than what we obtain from the Falcon observations.

[78] For comparison we also show results for the fine mode fraction measured at ground at Tinfou. Figure 4 shows the 24 hour mean volume size distribution of the fine mode fraction measured at Tinfou on 19 May 2006.

[79] The use of a PM-10 inlet limited the maximum detectable particle aerodynamic radius to 5 μm, which is equivalent to a geometric particle radius of 3.8 μm. It means that we cannot resolve the coarse mode fraction. However the fine mode of the particle size distribution, i.e., particles with radii up to approximately 1 μm, can be reliably detected with such a particle inlet system. Table 3 shows a factor of 3 less particles in the fine mode fraction compared to the AERONET results.

[80] In summary, particle sizing methods at ground and on board the Falcon yield similar total number concentrations although the data originate from different sites, Ouarzazate (Falcon) and Tinfou (ground-site). The AERONET results differ to both methods by almost the same factor.

[81] In this study we use a new AERONET measurement channel at 1638 nm. The new channel was not well-calibrated for this study, and may therefore introduce additional uncertainties of the derived data products. We estimate that uncertainty by analyzing our data with the AERONET retrieval algorithm including the data of the new measurement channel at 1638 nm, and a second time with the standard AERONET procedure excluding the channel at 1638 nm.

[82] Table 4 shows the percentage deviation of the parameters of the particle size distributions that may arise from using the new measurement channel. The parameters that we derive with and without the new measurement channel do not differ significantly. The differences are less than 5% in each case, and thus cannot be the reason for the strong differences between AERONET and Falcon results.

[83] The quality of the airborne size distributions measurements has been evaluated by *Weinzierl et al.* [2009] in the context of an intercomparison of particle extinction coefficients calculated from the in situ measured particle size distributions with the extinction coefficient measured directly with the HSRL. All calculations were done under the assumption of spherical particle shape, i.e., Mie-scattering theory was applied.

[84] With respect to the airborne measurements at 4853 m asl (3247 m asl), we find a deviation of 12% (7%) between the HSRL extinction coefficient measurements and the Mie-scattering calculations. The calculated values being higher. Considering the time off-set of about one hour between HSRL and in situ measurements and the rather low devia-

Table 4. Percentage Deviation of Particle Optical and Microphysical Parameters Determined From the AERONET Data Including the Measurement Channel at 1638 nm and Without the Channel at 1638 nm[a]

	Deviation (%)			
Parameter	Total	Fine Mode	Coarse Mode	
Effective radius	2.5	2.4	3.3	
Number concentration	−1.9	−2	11	
Surface-area concentration	−2.0	−1.1	−2.6	
Volume concentration	0.6	1.3	0.7	
	Deviation at Measurement Wavelength (%)			
Parameter	441 nm	675 nm	875 nm	1021 nm
Real part of complex refractive index	0.5	−0.3	0.1	0.3
Imaginary part of complex refractive index	−18.0	19.3	19.6	23.0

[a]Positive values indicate that the respective parameter is larger if the measurement channel at 1638 nm is used. With respect to mean and integral properties of the particle volume distribution we show the results for the total size distribution, for the fine mode fraction (below 0.5 μm particle radius), and for the coarse mode fraction (above 0.5 μm particle radius).

tion, both methods can be considered in good agreement for that specific day. *Weinzierl et al.* [2009] performed the extinction closure for other days. We find even better agreement for these measurements.

[85] The differences between AERONET retrievals and in situ aircraft measurements cannot be satisfactorily explained if our assumption of vertical and horizontal homogeneity of the observed dust plume is true. With regard to the aircraft in situ measurements we can also rule out that measurement uncertainties or problems with the instruments or the particle inlet system have lead to any significant reduction of the particle volume concentration.

[86] The volume size distributions as well as other parameters, e.g., complex refractive index, that are derived with the AERONET algorithm, are so-called *indirect* data products. That means these parameters are derived from the radiation fields that are observed with the instrument. The dust particle properties that we derive with the AERONET algorithm reproduce the measured angular (≈30 different angles) and spectral distribution of radiation (at the measurement wavelengths).

[87] For that reason, in a strict sense our comparison study is incomplete. A more complete way is that we also take particle size distributions measured aboard the Falcon aircraft, as well as the complex refractive index, feed them into the AERONET retrieval algorithm and simulate the corresponding radiation field that is observed with the AERONET instrument. Only this strict forward-backward validation study will hopefully give us final hints to the possible reason of the differences regarding the particle size distribution.

[88] The AERONET retrieval algorithm is not available to us. We are currently doing sensitivity studies with a different radiative transfer code for studying the radiation field.

3.3.2. Complex Refractive Index

[89] Figure 5 shows our results for the complex refractive index. Complex refractive indices of mineral dust have previously been presented by *Dubovik et al.* [2002a].

[90] We determined that parameter from our airborne in situ measurements in two ways. Analysis of the mineralogy of single particles which were collected with the aircraft, provides us with one set of numbers. We analyzed 12,900 particles in the particle radius range from 0.05 to 1.25 μm. The methodology is described in detail by *Kandler et al.* [2009]. In the following discussion we show that this technique does not suffer from the cut-off of large particles. Therefore, we believe that we obtain trustworthy numbers for the complex refractive index.

[91] The different symbols (dark blue, single-particle analysis aboard the Falcon) in Figure 5 denote the complex refractive index for different particle radius ranges. We show results for the radius range 0.05–0.25 μm (Figure 5, open triangle upward), 0.25–0.5 μm (Figure 5, open triangle downward), and 0.5–1.25 μm (Figure 5, open hexagon).

[92] We also analyzed the mineralogy of particles larger than 1.25 μm in radius (collected at the ground station at Tinfou). The different symbols (light blue) in Figure 5 denote the complex refractive index in the particle radius range of 0.05–0.25 μm (open triangle upward), 0.25–0.5 μm (open triangle downward), 0.5–1.25 μm (open hexagon), 1.25–2.5 μm (open diamond), 2.5–5 μm (open square), and 5–12.5 μm (open star).

[93] Below 0.25 μm particle radius we find a volume contribution of approximately 50% sulfate and 50% silicate [*Kandler et al.*, 2009], and a small volume contribution (in the low single digits) of soot [*Müller et al.*, 2009]. The chemical composition is not very variable for particle radii >0.25 μm up to 25 μm particle radius. Accordingly the various curves that are described with different symbols but same color are nearly on top of each other.

[94] We mostly find silicates, some contribution from quartz and calcite, and promilles of soot. Above 25 μm particle radius we find a volume contribution of 50% quartz.

[95] The results are similar for the aircraft measurements (Figure 5, dark blue curves). Thus, on the basis of the chemical composition, we should in fact find similar complex refractive indices of particles above and below 1.25 μm radius.

[96] The Sun photometer data and the in situ observations show that real and imaginary part depend on measurement wavelength. Figure 5a shows that the Sun photometer-derived mean values of the real part are significantly less than 1.5 throughout the range of measurement wavelengths. That result does not change, if we neglect in our analysis

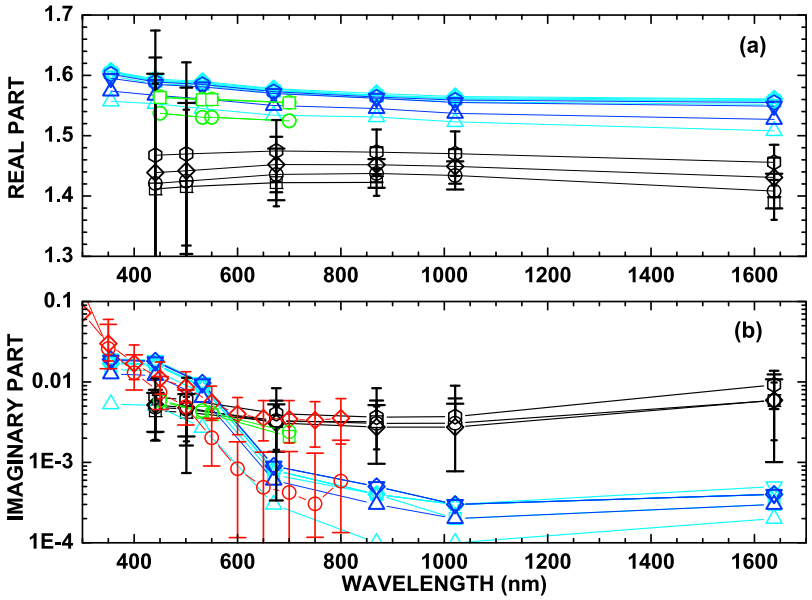

Figure 5. (a) Real part and (b) imaginary part of the complex refractive index determined from AERONET Sun photometer data (black symbols). The data points represent the measurements taken at 0649:19 UTC (open squares), 0711:50 UTC (open circles), 0801:35 UTC (open diamonds), and 0829:46 UTC (open hexagon). Complex refractive index derived from analysis of the mineralogy of single particles collected aboard the Falcon aircraft (dark blue symbols) and particles collected at Tinfou (light blue symbols). The different symbols denote the complex refractive index of different particle radius ranges, see main body of text. Complex refractive index (open green square: height range 4853 m asl; open green circle: height range 3247 m asl) obtained from the airborne in situ observations, see section 2.3. With the exception of the ground-based results at the Tinfou site, the parameters are only representative of particles with radii <1.25 μm. Imaginary part (red symbols) derived from observations of dust with an optical absorption spectrometer at Tinfou. One set of numbers follows from the total absorption coefficients (open red diamonds). The second set of numbers describes the contribution of pure dust (open red circles). The mean values denote the most likely values. The uncertainty bars describe extreme values, i.e., maximum and minimum reasonable value.

the Sun photometer data at 1638 nm, see Table 4. We find systematically higher values above 1.5 with the other measurement methods.

[97] Figure 5b shows the imaginary part of the refractive index. Above approximately 650 nm wavelength the imaginary parts determined from the AERONET algorithm (Figure 5b, black symbols) are higher than the imaginary parts determined from single-particle analysis of the mineralogy. The fact that the light blue and dark blue symbols are nearly on top of each other indicates that the mineralogy of particles collected aboard the Falcon and at ground at Tinfou is nearly the same.

[98] The wavelength-dependence of the imaginary part determined with the AERONET algorithm (Figure 5b, black symbols) for the wavelength range from 300 to 800 nm is less pronounced than the wavelength dependence that we obtain from the single-particle analysis of particle mineralogy (Figure 5b, dark blue and light blue symbols).

[99] This wavelength dependence of the imaginary part, derived with the AERONET instrument, becomes stronger if we neglect the measurement channel at 1638 nm, see Table 4. In that case the imaginary part is approximately 20% higher at 441 nm, whereas it decreases by approximately 20% at 675, 869, and 1021 nm.

[100] The Tinfou absorption spectrometer value at 450 nm (Figure 5b, red open square) is slightly larger than the AERONET result (observe that the scale of the y axis is logarithmic). The imaginary parts derived from the AERONET instrument and from SOAP agree well for the wavelength range from 500 to 800 nm. The imaginary parts from the Falcon measurements (Figure 5b, green open circles; 467, 530, and 660 nm) are also very similar to the results from the AERONET instrument. As mentioned, the Falcon data only present the particle size distribution up to a maximum particle radius of 1.25 μm, but according to single-particle analysis there are no significant differences of the mineralogy of particles below and above 1.25 μm radius.

[101] One striking feature in Figure 5b is the strong wavelength disparity of the imaginary parts obtained from the AERONET retrieval, the Falcon retrievals (Figure 5b, green symbols) and the SOAP data on the one hand, and the results from single-particle analysis on the other hand. One explanation may be as follows.

[102] The AERONET instrument, as well as the aircraft instruments and the SOAP instrument at Tinfou detect the total particle mixture. The total particle mixture, which is measured by the electron-microscopic single-particle analysis, includes nearly all of the inorganic components [*Kandler et al.*, 2009], and it may include strongly light-absorbing particles such as soot. The chemical analysis of the collected particles uses X-ray fluorescence methods [*Kandler et al.*,

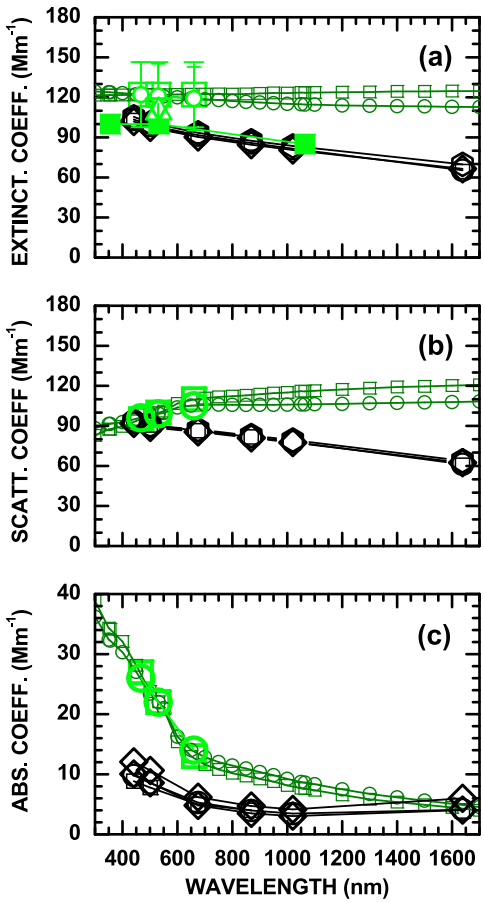

Figure 6. (a) Particle extinction, (b) scattering, and (c) absorption coefficients derived from AERONET Sun photometer measurements on 19 May 2006. Meaning of the black symbols is the same as before. Particle light-absorption coefficients were measured with the 3-wavelength PSAP aboard the Falcon aircraft (light green symbols). Particle scattering coefficients were calculated on the basis of Mie-scattering theory from the airborne-measured particle size distributions and the model described in section 2.3 (light green symbols). Extinction, scattering, and absorption coefficients derived from Mie-scattering computations with airborne-measured particle size distributions, up to particle radius 15 μm, are shown, too (dark green symbols). Shown are the results for the flight leg at 4853 m (open light green and dark green squares) and the flight leg at 3247 m height (open light green and dark green circles). Particle extinction coefficients were derived with the lidars at ground (closed squares). Particle extinction coefficients were measured with the airborne HSRL at 532 nm (downward pointing triangle for flight altitude at 3247 m, and upward pointing triangle for flight altitude at 4853 m).

2009], which are not able to resolve minute amounts of soot. Thus we only consider the pure dust contribution in the mineralogical single-particle analysis. The presence of soot is indicated by results from absorption photometry [*Müller et al.*, 2009; *Petzold et al.*, 2009] at the ground and in the air.

[103] *Müller et al.* [2009] show that for the ground-based measurements soot is a trace component and occurs for particles smaller than 500 nm only. This possible error source is corroborated by the following sensitivity test. If we correct the signals from the absorption spectrometer for the soot content we arrive at the open red circles which show better agreement to the results from microscopy analysis. A detailed description of that soot correction is given by *Müller et al.* [2009].

3.4. Extinction, Scattering, and Absorption Coefficients

[104] In this section we present particle extinction coefficients, particle scattering coefficients, particle absorption coefficients, and the Ångström exponents derived from the optical coefficients. The parameters describe particle surface-area-weighted properties of the investigated particle size distributions. Particle shape has only minor influence on the optical properties.

[105] As mentioned previously, the mineral dust plume was rather well mixed on 19 May 2006. The gradient of virtual potential temperature was zero in the dust plume, see also Figure 2. We do not expect that the mixing state of the dust plume is the main cause for differences of the parameters that we obtain from the column observations with Sun photometer, the vertical profiling with lidar, and the Falcon observations at different flight levels.

[106] As already stated in section 2 the extinction, scattering, and absorption coefficients are derived from the size distribution data, and rely on the input complex refractive index data from literature. For the visible spectral range we find good agreement. Comparison with HSRL data indicate an uncertainty <20%.

[107] Literature values of the complex refractive index may be affected with strong errors at the infrared wavelengths. There are no independent optical data available for a quality assurance of the optical properties that we calculated with Mie-scattering theory.

[108] Figure 6 shows column-mean particle extinction coefficients measured with Sun photometer. Also shown are the column-mean values of the particle scattering and the particle absorption coefficients. We obtain the latter two quantities on the basis of the derived particle size distributions and the complex refractive indices. We calculated the mean values by using a geometrical depth of 3600 m for the dust plume, see Figure 3.

[109] Particle extinction coefficients were measured with the rotational Raman channels of the BERTHA lidar and the high-spectral-resolution channels of the Falcon lidar at 532 nm, see Figure 3. These profiles can be retrieved down to the ground. We calculated mean extinction values at 355 nm and 1064 nm on the basis of measurements of the elastic backscatter signals with all four lidar systems. The values at 355 nm are obtained with the assumption of a particle extinction-to-backscatter ratio of 53 sr. The numbers at 1064 nm are calculated with the assumption of a particle extinction-to-backscatter ratio of 55 sr. We find excellent agreement of the dust-column-mean particle extinction coefficient measured with the AERONET Sun photometer and with our lidar systems.

[110] Figure 6 shows particle extinction coefficients derived from airborne measurements (the light green and dark green symbols). The data are available for the two flight altitudes at 3247 and 4853 m asl. We scaled the numbers of

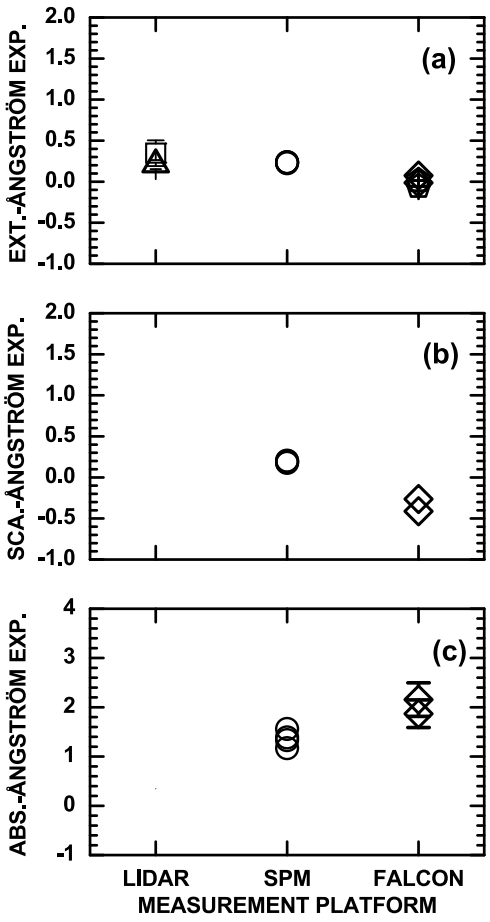

Figure 7. Particle Ångström exponents derived from (a) the particle extinction, (b) the particle scattering, and (c) the particle absorption coefficients shown in Figure 6. We use the following wavelength pairs for our comparison: 355/532 nm (lidar; square) and 532/1064 nm (lidar; triangle), 441/869 nm (AERONET Sun photometer (SPM); circles), and 467/660 nm (Falcon; diamonds).

the optical parameters to ambient atmospheric conditions [*Weinzierl et al.*, 2009]. The airborne extinction measurements at the three measurement wavelengths of the PSAP are approximately 7%–12% larger than the extinction coefficients measured with Sun photometer and lidar.

[111] Mie-scattering calculations on the basis of the entire particle size distribution measured aboard the Falcon and AERONET results for dust extinction and scattering coefficients show large differences in the near infrared spectral region. In contrast we find good agreement in the visible spectral region. This wavelength-dependent difference suggests that the complex-refractive-index data derived with the AERONET algorithm or the refractive indices used in the Mie-scattering calculations require improvements in the near infrared wavelength range.

[112] The imaginary part of the complex refractive index that is derived with the AERONET algorithm agrees well with the value that is used for the Mie-scattering calculations. The strong difference in the absorption coefficients may be largely attributed to the differences in the underlying particle size distributions.

[113] Figure 7 compares shape-independent intensive particle optical properties, i.e. Ångström exponents for particle extinction, scattering, and absorption for different wavelength pairs. The choice of wavelength pairs is constrained by the measurement wavelengths of the various measurement platforms. We believe that a quality test of the Ångström exponents from the various measurement platforms is possible as the wavelength pairs are similar enough.

[114] Ångström exponents of particle extinction measured with Sun photometer and derived from the daytime Raman lidar observations agree well. In the case of the Raman lidar we use the daytime profiles of the particle backscatter coefficients and lidar ratios measured at nighttime. The lidar ratios measured during SAMUM are nearly wavelength independent. The two methods deliver Ångström exponents between 0 and 0.5.

[115] The same range of numbers is found for the scattering Ångström exponents which follow from the AERONET retrievals (see Figure 7b). The Ångström exponents derived from the Falcon measurements resulted, on average, in lower numbers for the wavelength interval 450–700 nm. We obtain slightly negative values from the Falcon aircraft measurements, i.e., 0 to −0.5.

[116] With regard to the Ångström exponents of particle absorption we find values of around 1.5 from the inversion of the Sun photometer data. Values of around 2 are derived from the data acquired with the Falcon aircraft.

3.4.1. Single-Scattering Albedo

[117] Figure 8 shows single-scattering albedo. The AERONET observations result in a single-scattering albedo of ≈0.9 at 441 and 501 nm. The single-scattering albedo increases to ≈0.95 at near-infrared wavelengths, and then drops again to 0.9–0.95 at 1638 nm wavelength. We obtain nearly the same values for single-scattering albedo from the absorption spectrometer measurements at Tinfou.

[118] Single-scattering albedo at 1638 nm is noticeably lower than the values at 871 and 1021 nm. We believe that this difference is caused by the higher calibration uncertainty of the infrared channel, particularly if we take into account that aerosol optical depth is lower at 1638 nm compared to optical depth at the other wavelengths.

[119] Moreover, this uncertainty can propagate and affect the retrieval results at the other measurement wavelengths. We find slightly different values of single-scattering albedo,

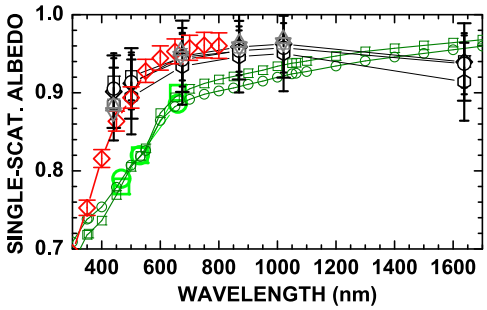

Figure 8. Single-scattering albedo determined from AERONET Sun photometer data, Falcon in situ measurements of particle size distributions, and SOAP. Color key and data description as in Figure 5. Scattering coefficients were calculated using Mie-scattering theory [*Müller et al.*, 2009].

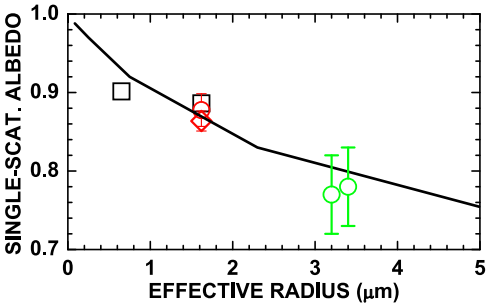

Figure 9. Single-scattering albedo at the wavelength of 450 nm determined from AERONET (black squares), from Mie-scattering calculations as a function of the effective radius of the probed aerosol particles (green circles representing the two flight altitudes), and from the measurements at Tinfou (red circle for the soot corrected value, and red diamond for the uncorrected value). The AERONET results are shown for the effective radius of the total particle size distribution, and also for the coarse mode fraction of the dust size distribution, see Table 3. The solid line represents the parametrization of the dependence of the single-scattering albedo on effective radius [*Tegen et al.*, 2006] for dust from the Bodélé depression.

if we derive that parameter with the AERONET standard retrieval algorithm which does not use data at 1638 nm, see Table 4.

[120] The results from the Mie-scattering calculations (Falcon) are consistently the smallest values. The different single-scattering albedo values are mainly related to the different particle size ranges considered in our study.

[121] Figure 9 shows the influence of the size range on single-scattering albedo. Following the dependence of the single-scattering albedo on the effective radius of dust [*Tegen et al.*, 2006], the single-scattering albedo decreases with increasing particle size for a constant refractive index. We may scale the results of the Mie-scattering calculations for the effective radius of around 3–3.5 μm (measured aboard the Falcon) to the value of 0.23 μm (reported for the Tinfou site). This scaling shifts the single-scattering albedo at 450 nm from 0.77 (total aerosol size distribution) to approximately 0.90 for the PM-10 aerosol. This scaled value is in close agreement with the values reported from the ground-site and the AERONET measurements.

4. Discussion

[122] In this contribution we compare optical and microphysical properties of Saharan mineral dust observed in Morocco during SAMUM 2006. Goal of this study is to identify limitations of the measurement capabilities of the various platforms and contradictions in the measured parameters. We use the measurement on 19 May 2006 as a case study. This measurement day was chosen as a case study because it delivers high quality data from all SAMUM stations involved in this study. One case study by far is not enough to draw general conclusions on the performance of the various stations. A statistical analysis still needs to be done. The work carried out in the framework of this case study provides us with the necessary insight for a more thorough analysis of additional measurement days.

[123] We obtain agreement but also in part disagreement for the various dust parameters. Time and space separation between ground-based lidar, AERONET, and in situ aircraft measurements is negligible since the flight patterns were designed such that an overflight over the ground lidar and AERONET station was possible. Remote sensing of the dust layer by the airborne lidar requires overflight of the layer whereas in situ sampling requires flying inside the layer. For that reason there is a time shift. Data acquired with the stationary ground lidars show that there were no significant changes of dust properties during the probing. The differences between the methods cannot be attributed to time and space separation of the sampling but rather to methodological differences.

[124] In the following we first summarize the results for the fundamental microphysical parameters, i.e., particle size distribution and complex refractive index. Then we discuss our findings for the shape-independent optical properties, i.e., extinction, scattering and absorption coefficients, Ångström exponents that can be derived from these extensive optical particle properties, and single-scattering albedo.

[125] Particle volume size distributions retrieved with the AERONET algorithm and measured aboard the Falcon aircraft are different. Particle effective radius from the AERONET algorithm turns out to be smaller, if we calculate that same parameter from the complete size distribution measured aboard the aircraft. On that day particles with maximum radius of around 15 μm were detected aboard the Falcon. The AERONET algorithm also uses particles with radii up to 15 μm in the data analysis. Both methodologies use rather similar lower limits of the particle radius in the data analysis.

[126] The lower effective radius from AERONET is caused by a lower volume concentration of particles in the coarse mode fraction of the particle size distribution (particle radius from 0.5 to 15 μm). We also find differences in the fine mode fraction, i.e., below 0.5 μm particle radius. The airborne observations show a much lower (factor 2.5–3) number concentration of particles in the fine mode. Ground-based in situ measurements of particle size distributions at the second field site of SAMUM 2006 at Tinfou also show a factor 3 lower number concentration of particles in the fine mode fraction of the size distribution. Up to this point we cannot explain the observed differences. Further sensitivity tests, e.g., radiative transfer simulations are underway.

[127] We find differences with regard to the real part of the complex refractive index. The AERONET results show values below 1.5 throughout the used measurement wavelength range (441–1638 nm). In contrast, we find values of 1.5–1.6 from the analysis of the chemical composition of several thousand particles collected at ground at Tinfou as well as collected aboard the Falcon aircraft. We identified the pure elements and used tabulated values of these pure substances to determine the real part of the particles. Although in some cases these tables are rather old, we do not believe that the tabulated values are responsible for the observed differences. We find similar results for the real part from the PSAP inversion scheme that was applied to the airborne dust measurements.

[128] The imaginary part that is derived from the AERONET instrument for wavelengths below 600 nm is lower than what we obtain in that same wavelength range

from the chemical analysis of single particles. At the same time we find higher values from AERONET than from single-particle analysis for wavelengths above 600 nm. Single-particle analysis only considered pure mineral dust particle. The AERONET instrument may have detected traces of other particle substances which may lead to differences in the observed imaginary part. This assumption is corroborated by SOAP measurements at Tinfou [*Müller et al.*, 2009].

[129] We also derived the imaginary part from airborne observations of particle size distributions, light-absorption measurements, and volatility analyses with aid of an aerosol optical model. Imaginary parts from the Falcon instrument agree to the ones from the AERONET retrievals.

[130] Extinction coefficients are calculated with Mie-scattering theory, i.e., spherical particle shape is assumed, from particle size distributions measured aboard the Falcon aircraft and the use of complex refractive indices that were derived for the wavelength range from 467 to 660 nm. We find extinction coefficients which are approximately 10% larger for the Falcon-computed results between 467 and 660 nm, compared to the extinction coefficients measured by lidar and Sun photometer. We find 60% larger values, compared to the Sun photometer measurements, at infrared wavelengths around 1600 nm.

[131] Sun photometer optical depths are typically measured to fairly high accuracies (better than 1%). Particle extinction coefficients derived from Sun photometer optical depths have low uncertainty, as we know the dust layer geometrical depth from our lidar instruments fairly well. The Mie-scattering calculations show strong deviations at wavelengths larger than 660 nm. In our opinion these deviations are caused by errors of the complex refractive indices that were used in the calculations. The complex refractive indices for the infrared wavelength range were taken from literature, as discussed by *Petzold et al.* [2009]. This result indicates the need for a better knowledge of complex refractive indices at infrared wavelengths.

[132] We also find deviations between particle scattering and particle absorption coefficients from Sun photometer and from the airborne data. The reason for the difference again may in large part be caused by inaccurate complex refractive indices (in the infrared wavelength range) that had to be taken for the analysis of the Falcon data.

[133] Particle absorption and scattering coefficients from the AERONET instrument are not measured directly. Those parameters follow from the derived quantities of particle phase functions, complex refractive indices, and particle size distributions. Therefore, some of the deviations may also be attributed to uncertainties of the AERONET algorithm.

5. Outlook

[134] We are not clear about the contributions of the different measurement platforms to the observed discrepancies. Up to this point we compare data products for one specific measurement day.

[135] To clarify this situation we have to analyze additional measurement days. For a more detailed comparison study we may use all the days on which we had overflights by the Falcon aircraft. There were seven such days, of which six were relevant for the lidar observations. We shall also use data from our ground-based instruments where appropriate. In addition we have 27 days for which AERONET delivers microphysical properties of dust. Those days will add statistical information to the derived data products.

[136] We restricted our analysis to standard data products of the AERONET algorithm, i.e. particle size distributions, complex refractive indices, and shape-independent optical dust properties. In future we also need to separate the data products according to the fine mode and coarse mode fraction of the total particle size distribution.

[137] We shall carry out a much stricter evaluation of the data products from the various measurement platforms by comparing particle-shape dependent dust properties. Such properties are for instance phase function, backscatter coefficients, lidar ratios, depolarization ratios, and aspect ratios. We believe that such a comparison study will give us much clearer indication on the possible error sources the various measurement platforms are affected with. SAMUM 2006 provides us for the first time with the data set needed for a benchmark test of shape-dependent dust optical and microphysical properties. First results are presented by *Müller et al.* [2010].

Appendix A

[138] The results from the AERONET Sun photometer (Figures 5, 6, 8, and 9, black color, open symbols) always refer to the total particle size distribution unless otherwise indicated.

[139] The results from in situ measurements of the Falcon aircraft are kept in light green for data at wavelengths at which we measured with the PSAP. We use dark green color and open symbols for wavelengths that we use for additional Mie-scattering calculations.

[140] The data from single-particle analysis are kept in dark blue and open symbols if particles were collected aboard the Falcon aircraft. We use light blue color and open symbols to present data from particles that were collected near ground at Tinfou.

[141] The results from the particle light-absorption photometer that was operated at Tinfou are presented in red colors and open symbols. The data from lidar are kept in light-green colors and closed symbols for the ground-based systems.

[142] Furthermore each color-coded set of results (open symbols) also uses various shapes of symbols. The different symbols of each color code either denote different measurement times or height levels for which data were acquired with the respective platform. In some cases a different data analysis technique was applied to the available data set from a given measurement platform. The results from the different analysis techniques for the same platform also are presented with different symbols but in the same color.

[143] We chose a separate symbol notation (compared to the ground-based systems) for the airborne HSRL system. Those data are denoted with light-green, open triangles.

[144] **Acknowledgments.** This work was funded by the Korea Meteorological Administration Research and Development Program under Grant CATER 2009-3112. The SAMUM consortium was funded by the German Research Foundation (Deutsche Forschungsgemeinschaft) within the Research Group SAMUM under grant FOR 539. We thank Oleg Dubovik and the AERONET team at Goddard Space Flight Center

for providing us with high-quality Sun photometer results. We are grateful to the Moroccan Ministry for Foreign Affairs and the Ministry of the Interior for the permission to carry out the SAMUM field campaign in Morocco. We thank the Moroccan Airport Authority and in particular respectable Monsieur Mohammed El Mardi, commander of Ouarzazate airport, for their extraordinary support of the participants of SAMUM. Detlef Müller would like to thank L. T. for the great support.

References

Ackermann, T. P., and O. B. Toon (1981), Absorption of visible radiation in atmosphere containing mixtures of absorbing and nonabsorbing particles, *Appl. Opt.*, *20*, 3661–3667.

Althausen, D., D. Müller, A. Ansmann, U. Wandinger, H. Hube, E. Clauder, and S. Zörner (2000), Scanning 6-wavelength 11-channel aerosol lidar, *J. Atmos. Oceanic Technol.*, *17*, 1469–1482.

Ångström, A. (1964), The parameters of atmospheric turbidity, *Tellus*, *16*, 64–75.

Ansmann, A., and D. Müller (2005), Lidar and atmospheric aerosol particles, in *Lidar. Range-Resolved Optical Remote Sensing of the Atmosphere*, edited by C. Weitkamp, pp. 105–141, Springer, New York.

Bierwirth, E., et al. (2009), Spectral surface albedo over Morocco and its impact on the radiative forcing of Saharan dust, *Tellus Ser. B*, *61*, 252–269.

Bohren, C. F., and D. R. Huffman (Eds.) (1983), *Absorption and Scattering of Light by Small Particles*, 530 pp., John Wiley, Hoboken, N. J.

Borrmann, S., B. Luo, and M. Mishchenko (2000), Application of the T-matrix method to the measurement of aspherical (ellipsoidal) particles with forward scattering optical particle counters, *J. Atmos. Sci.*, *31*, 789–799.

Deuzé, J. L., P. Gloub, M. Herman, A. Marchand, G. Perry, S. Susana, and D. Tanré (2000), Estimate of the aerosols properties over the ocean with POLDER, *J. Geophys. Res.*, *105*, 15,329–15,346.

Dubovik, O., and M. D. King (2000), A flexible inversion algorithm for retrieval of aerosol optical properties from Sun and sky radiance measurements, *J. Geophys. Res.*, *105*, 20,673–20,696.

Dubovik, O., A. Smirnov, B. N. Holben, M. D. King, Y. J. Kaufman, T. F. Eck, and I. Slutsker (2000), Accuracy assessments of aerosol optical properties retrieved from Aerosol Robotic Network (AERONET) Sun and sky radiance measurements, *J. Geophys. Res.*, *105*, 9791–9806.

Dubovik, O., B. N. Holben, T. F. Eck, A. Smirnov, Y. J. Kaufman, M. D. King, D. Tanré, and I. Slutsker (2002a), Variability of absorption and optical properties of key aerosol types observed in worldwide locations, *J. Atmos. Sci.*, *59*, 590–608.

Dubovik, O., B. N. Holben, T. Lapyonok, A. Sinyuk, M. I. Mishchenko, P. Yang, and I. Slutsker (2002b), Non-spherical aerosol retrieval method employing light scattering by spheroids, *Geophys. Res. Lett.*, *29*(10), 1415, doi:10.1029/2001GL014506.

Dubovik, O., et al. (2006), The application of spheroid models to account for aerosol particle nonsphericity in remote sensing of desert dust, *J. Geophys. Res.*, *111*, D11208, doi:10.1029/2005JD006619.

Eloranta, E. W. (2005), High spectral resolution lidar, in *Lidar. Range-Resolved Optical Remote Sensing of the Atmosphere*, edited by C. Weitkamp, pp. 143–163, Springer, New York.

Esselborn, M., M. Wirth, A. Fix, B. Weinzierl, K. Rasp, M. Tesche, A. Petzold, and G. Ehret (2009), Spatial distribution and optical properties of Saharan dust observed by airborne high spectral resolution lidar during SAMUM 2006, *Tellus Ser. B*, *61*, 131–143.

Freudenthaler, V., et al. (2009), Depolarization-ratio profiling at several wavelengths in pure Saharan dust during SAMUM 2006, *Tellus Ser. B*, *61*, 165–179.

Grund, C. J., and E. W. Eloranta (1990), The 27–28 October 1986 Fire IFO Cirrus case-study—Cloud optical-properties determined by High Spectral Resolution Lidar, *Mon. Weather Rev.*, *118*, 2344–2355.

Hamonou, E., P. Chazette, D. Balis, F. Dulac, X. Schneider, E. Galani, G. Ancellet, and A. Papayannis (1999), Characterization of the vertical structure of Saharan dust export to the Mediterranean basin, *J. Geophys. Res.*, *104*, 22,257–22,270.

Heintzenberg, J. (1978), Particle size distributions from scattering measurements of nonspherical particles via Mie-theory, *Contrib. Atmos. Phys.*, *51*, 91–99.

Herman, M., J. L. Deuzé, A. Marchand, B. Roger, and P. Lallart (2005), Aerosol remote sensing from POLDER/ADEOS over the ocean: Improved retrieval using a nonspherical particle model, *J. Geophys. Res.*, *110*, D10S02, doi:10.1029/2004JD004798.

Holben, B. N., et al. (1998), AERONET—A federated instrument network and data archive for aerosol characterization, *Remote Sens. Environ.*, *66*, 1–16.

Holben, B. N., et al. (2001), An emerging ground-based aerosol climatology: Aerosol optical depth from AERONET, *J. Geophys. Res.*, *106*, 12,067–12,097.

Kahn, R., R. West, D. McDonald, B. Rheingans, and M. I. Mishchenko (1997), Sensitivity of multiangle remote sensing observations to aerosol sphericity, *J. Geophys. Res.*, *102*, 16,861–16,870.

Kalashnikova, O. V., and I. N. Sokolik (2002), Importance of shapes and compositions of wind-blown dust particles for remote sensing at solar wavelengths, *Geophys. Res. Lett.*, *29*(10), 1398, doi:10.1029/2002GL014947.

Kalashnikova, O. V., and I. N. Sokolik (2004), Modeling the radiative properties of nonspherical soil-derived mineral aerosols, *J. Quant. Spectrosc. Radiat. Transfer*, *87*, 137–166.

Kalashnikova, O. V., R. Kahn, I. N. Sokolik, and W.-H. Li (2005), Ability of multiangle remote sensing observations to identify and distinguish mineral dust types: Optical models and retrievals of optically thick plumes, *J. Geophys. Res.*, *110*, D18S14, doi:10.1029/2004JD004550.

Kandler, K., et al. (2009), Size distribution, mass concentrations, chemical and mineralogical composition, and derived optical parameters of the boundary layer at Tinfou, Morocco, during SAMUM 2006, *Tellus Ser. B*, *61*, 32–50.

Kaufman, Y. J. (1993), Aerosol optical-thickness and atmospheric path radiance, *J. Geophys. Res.*, *98*, 2677–2692.

Knippertz, P., et al. (2009), Dust mobilization and transport in the northern Sahara during SAMUM 2006: A meteorological overview, *Tellus Ser. B*, *61*, 12–31.

Krotkov, N. A., D. E. Flittner, A. J. Krueger, A. Kostinski, C. Riley, W. Rose, and O. Torres (1999), Effect of particle nonsphericity on satellite monitoring of drifting volcanic ash clouds, *J. Quant. Spectrosc. Radiat. Transfer*, *63*, 613–630.

Lacis, A. A., and M. I. Mishchenko (1995), *Climate Forcing, Climate Sensitivity, and Climate Response: A Radiative Modeling Perspective on Atmospheric Aerosols*, pp. 11–42, John Wiley, Hoboken, N. J.

Liu, Y. G., W. P. Arnott, and J. Hallett (1999), Particle size distribution retrieval from multispectral optical depth: Influences of particle nonsphericity and refractive index, *J. Geophys. Res.*, *104*, 31,753–31,762.

McConnell, C. L., et al. (2008), Seasonal variations of the physical and optical characteristics of Saharan dust: Results from the Dust Outflow and Deposition to the Odean (DODO) experiment, *J. Geophys. Res.*, *113*, D14S05, doi:10.1029/2007JD009606.

Mishchenko, M. I., L. D. Travis, R. A. Kahn, and R. A. West (1997), Modeling phase functions for dustlike tropospheric aerosols using a shape mixture of randomly oriented polydisperse spheroids, *J. Geophys. Res.*, *102*, 16,831–16,847.

Mishchenko, M. I., W. J. Wiscombe, J. W. Hovenier, and L. D. Travis (2000), Overview of scattering by nonspherical particles, in *Light Scattering by Nonspherical Particles: Theory, Measurements, and Applications*, edited by M. I. Mishchenko, L. D. Travis, and J. W. Hovenier, pp. 29–60, Academic, San Diego, Calif.

Mishchenko, M. I., I. V. Geogdzhayev, L. Liu, J. A. Ogren, A. A. Lacis, W. B. Rossow, J. W. Hovenier, H. Volten, and O. Muñoz (2003), Aerosol retrievals from AVHRR radiances: Effects of particle non-sphericity and absorption and an updated long-term climatology of aerosol properties, *J. Quant. Spectrosc. Radiat. Transfer*, *79–80*, 953–972.

Müller, D., I. Mattis, U. Wandinger, D. Althausen, A. Ansmann, O. Dubovik, S. Eckhardt, and A. Stohl (2003), Saharan dust over a Central European EARLINET-AERONET site: Combined observations with Raman lidar and Sun photometer, *J. Geophys. Res.*, *108*(D12), 4345, doi:10.1029/2002JD002918.

Müller, D., et al. (2010), Mineral dust observed with AERONET Sun photometer, Raman lidar, and in situ instruments during SAMUM 2006: Shape-dependent particle properties, *J. Geophys. Res.*, doi:10.1029/2009JD012523, in press.

Müller, T., A. Schladitz, A. Maßling, N. Kaaden, A. Wiedensohler, and K. Kandler (2009), Spectral absorption coefficients and imaginary parts of refractive indices of Saharan dust during SAMUM-1, *Tellus Ser. B*, *61*, 79–95.

Nakajima, T., M. Tanaka, M. Yamamoto, M. Shiobara, K. Arao, and Y. Nakanishi (1989), Aerosol optical characteristics in the Yellow Sand events observed in May 1982 at Nagasaki: Part II. Models, *J. Meteorol. Soc. Jpn.*, *67*, 279–291.

Osborne, S. R., B. T. Johnson, J. M. Haywood, A. J. Baran, M. A. J. Harrison, and C. L. McConnel (2008), Physical and optical properties of mineral dust aerosol during the Dust and Biomass-burning Experiment, *J. Geophys. Res.*, *113*, D00C03, doi:10.1029/2007JD009551.

Petzold, A., et al. (2009), Saharan dust refractive index and optical properties from aircraft-based observations during SAMUM 2006, *Tellus Ser. B*, *61*, 118–130.

Schladitz, A., T. Müller, N. Kaaden, K. Kandler, and A. Wiedensohler (2009), Measurements of in situ optical properties at Tinfou (Morocco) during the Saharan Mineral Dust Experiment SAMUM 2006, *Tellus Ser. B*, *61*, 64–78.

Sinyuk, A., O. Torres, and O. Dubovik (2003), Combined use of satellite and surface observations to infer the imaginary part of Saharan dust, *Geophys. Res. Lett.*, *30*(2), 1081, doi:10.1029/2002GL016189.

Tegen, I., B. Heinold, M. Todd, J. Helmert, R. Washington, and O. Dubovik (2006), Modelling soil dust aerosol in the Bodele depression during the BoDEx campaign, *Atmos. Chem. Phys.*, *6*, 4345–4359.

Tesche, M., et al. (2009), Vertical profiling of Saharan dust with Raman lidars and airborne HSRL in southern Morocco during SAMUM, *Tellus Ser. B*, *61*, 144–164.

Toledano, C., M. Wiegner, M. Garhammer, M. Seefeldner, V. Freudenthaler, J. Gasteiger, D. Müller, and P. Koepke (2009), Spectral aerosol optical depth characterization of desert dust during SAMUM 2006, *Tellus Ser. B*, *61*, 216–228.

Virkkula, A., N. Ahlquist, D. Covert, P. Sheridan, W. Arnott, and J. Ogren (2005), A three-wavelength optical extinction cell for measuring aerosol light extinction and its application to determining light absorption coefficient, *Aerosol Sci. Technol.*, *39*, 52–67.

Volten, H., O. Muñoz, E. Rol, J. F. de Haan, W. Vassen, J. W. Hovenier, K. Muinonen, and T. Nousiainen (2001), Scattering matrices of mineral aerosol particles at 441.6 and 632.8 nm, *J. Geophys. Res.*, *106*, 17,375–17,401.

Wang, J., X. Liu, S. A. Christopher, J. S. Reid, E. Reid, and H. Maring (2003), The effects of non-sphericity on geostationary satellite retrievals of dust aerosols, *Geophys. Res. Lett.*, *30*(24), 2293, doi:10.1029/2003GL018697.

Weinzierl, B., A. Petzold, M. Esselborn, M. Wirth, K. Rasp, K. Kandler, L. Schütz, P. Köpke, and M. Fiebig (2009), Airborne measurements of dust layer properties, particle size distribution and mixing state of Saharan dust during SAMUM 2006, *Tellus Ser. B*, *61*, 96–117.

West, R. A., L. R. Doose, A. M. Eibl, M. G. Tomasko, and M. I. Mishchenko (1997), Laboratory measurements of mineral dust scattering phase function and linear depolarization, *J. Geophys. Res.*, *102*, 16,871–16,881.

Wiegner, M., et al. (2009), Numerical simulations of optical properties of Saharan dust aerosols with emphasis on linear depolarization ratio, *Tellus Ser. B*, *61*, 180–194.

D. Althausen, A. Ansmann, B. Heese, D. Müller, T. Müller, A. Schladitz, and M. Tesche, Leibniz Institute for Tropospheric Research, Permoserstr. 15, D-04318 Leipzig, Germany. (dietrich@tropos.de; albert@tropos.de; heese@tropos.de; detlef@tropos.de; muellert@tropos.de; schlax@tropos.de; tesche@tropos.de)

M. Esselborn, A. Petzold, and B. Weinzierl, Institut für Physik der Atmosphäre, Deutsches Zentrum für Luft- und Raumfahrt, Oberpfaffenhofen, D-82234 Wessling, Germany. (michael.esselborn@dlr.de; andreas.petzold@dlr.de; bernadett.weinzierl@dlr.de)

V. Freudenthaler, Meteorological Institute, Ludwig Maximilian University, Theresienstr. 37, D-80333 Munich, Germany. (volker.freudenthaler@meteo.physik.uni-muenchen.de)

K. Kandler, Institut für Angewandte Geowissenschaften, Technische Universität Darmstadt, D-64287 Darmstadt, Germany. (kzk@gmx.de)

P. Knippertz, School of Earth and Environment, University of Leeds, Leeds LS2 9JT, UK. (p.knippertz@leeds.ac.uk)

S. Otto, Institut für Methodik der Fernerkundung, Deutsches Zentrum für Luft- und Raumfahrt, Oberpfaffenhofen, D-82234 Wessling, Germany. (sebastian.otto@dlr.de)